Supporting Information

Tailoring the selectivity of ultralow-power heterojunction gas sensors by noble metal nanoparticle functionalization

Oleg Lupan [a,b,c,d,*], Nicolai Ababii [b], David Santos-Carballal [e,*], Maik-Ivo Terasa [a], Nicolae Magariu [b], Dario Zappa [f], Elisabetta Comini [f], Thierry Pauporte [c], Leonard Siebert [a], Franz Faupel [g,*], Alexander Vahl [g,*], Sandra Hansen [a,*], Nora H de Leeuw [e,h], and Rainer Adelung [a,*]

[a] *Functional Nanomaterials, Faculty of Engineering, Institute for Materials Science, Kiel University, Kaiserstr. 2, D-24143, Kiel, Germany*

[b] *Center for Nanotechnology and Nanosensors, Department of Microelectronics and Biomedical Engineering, Technical University of Moldova, 168 Stefan cel Mare Av., MD-2004 Chisinau, Republic of Moldova*

[c] *PSL Université, Institut de Recherche de Chimie Paris-IRCP, Chimie ParisTech, rue Pierre et Marie Curie 11, 75231 Paris Cedex 05, France*

[d] *Department of Physics, University of Central Florida, Orlando, FL 32816-2385, USA*

[e] *School of Chemistry, University of Leeds, Leeds LS2 9JT, United Kingdom*

[f] *Sensor Laboratory, Department of Information Engineering (DII), University of Brescia, Via Branze 38, Brescia 25123, Italy*

[g] *Chair for Multicomponent Materials, Faculty of Engineering, Kiel University, Kaiserstr. 2, D-24143, Kiel, Germany*

[h] *Department of Earth Sciences, Utrecht University, Princetonplein 8A, 3584 CD Utrecht, The Netherlands*

*Corresponding authors:
Rainer Adelung (ra@tf.uni-kiel.de),

Oleg Lupan (ollu@tf.uni-kiel.de , oleg.lupan@mib.utm.md), Dr. David Santos-Carballal (d.santos-carballal@leeds.ac.uk) Dr. Alexander Vahl (alva@tf.uni-kiel.de), Dr. Sandra Hansen (sn@tf.uni-kiel.de)
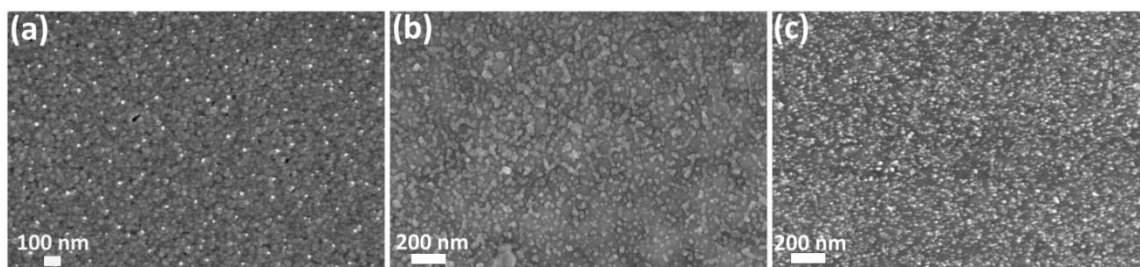
Figure S1. Scanning electron microscopy (SEM) images of the: (a) CuO/Cu$_2$O; (b) TiO$_2$/CuO/Cu$_2$O; and (c) AgPt/TiO$_2$/CuO/Cu$_2$O samples with a CuO/Cu$_2$O thickness of 20 nm.
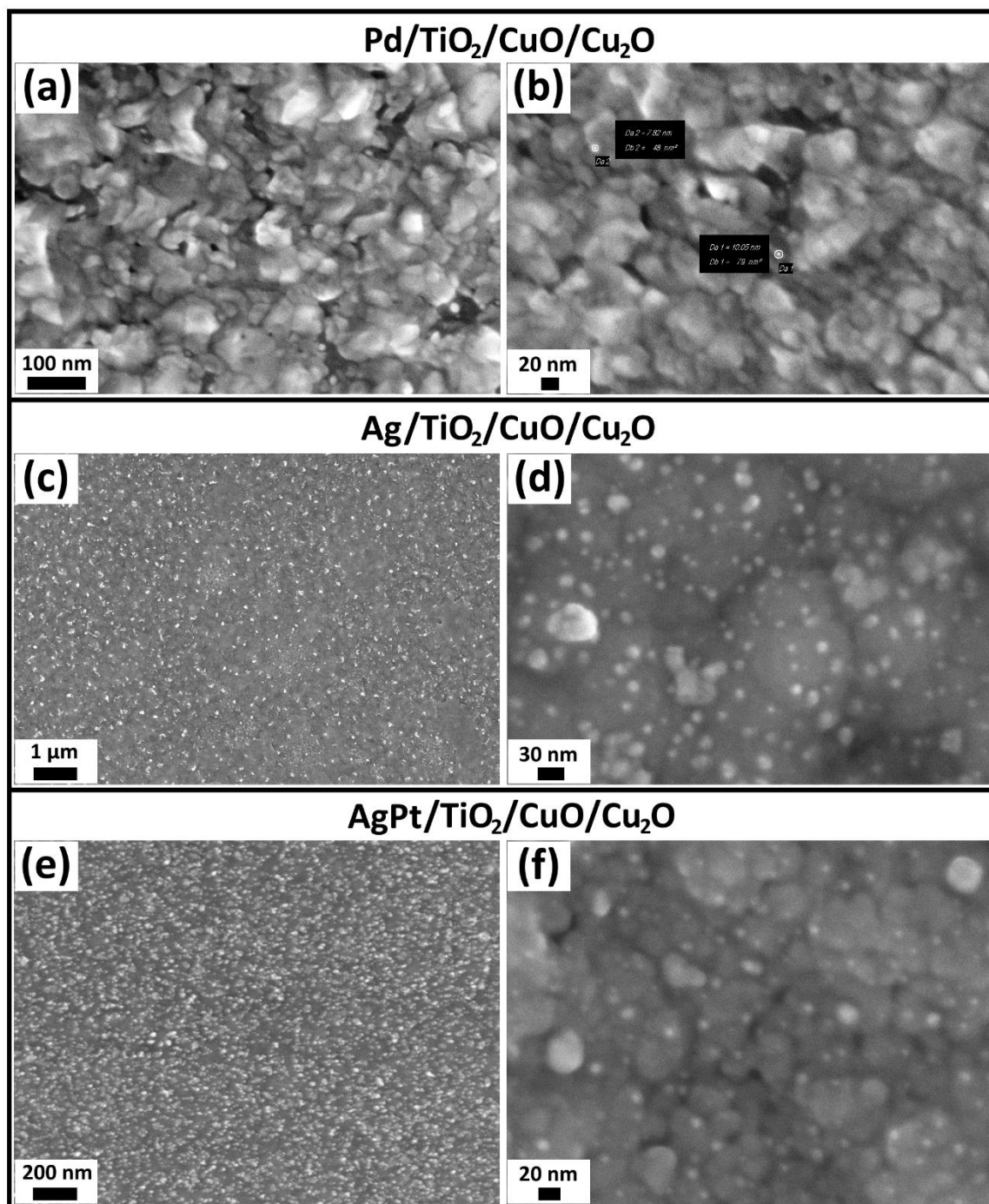
Figure S2. Scanning electron microscopy (SEM) images of $TiO_2/CuO/Cu_2O$ samples covered with Pd nanoclusters at: (a) low and (b) high magnification; Ag nanoclusters at (c) low and (d) high magnification; and AgPt nanoclusters at (a) low and (b) high magnification.
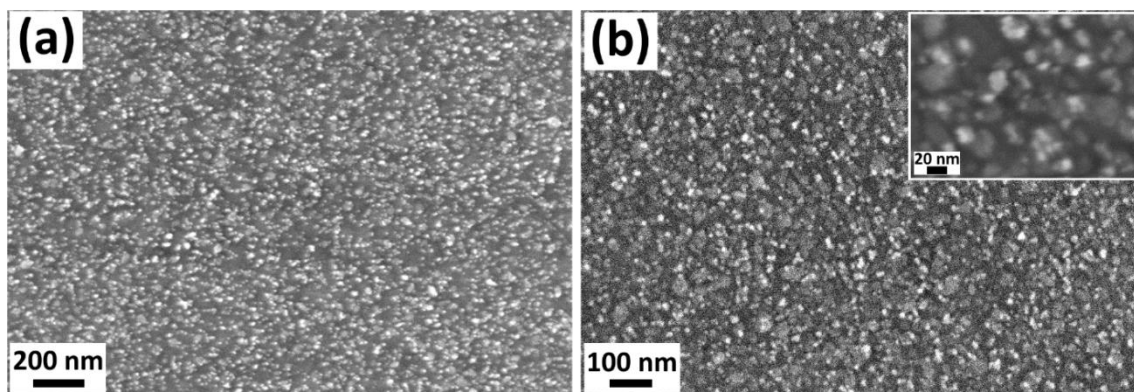
Figure S3. (a) Low and (b) high magnification of scanning electron microscopy (SEM) images of interconnected nano-crystallite $TiO_2/CuO/Cu_2O$ set sample with a CuO/Cu_2O thickness of 20 nm covered with AgPt nanoclusters of 5-15 nm in diameter. Inset in (b) shows an area of about 160×200 nm of sample from (b).
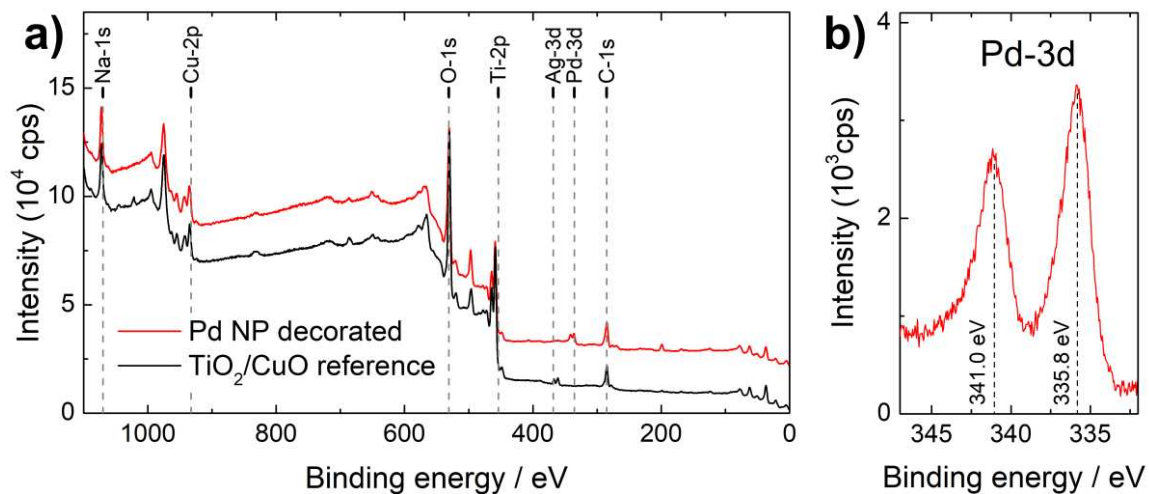
Figure S4. X-ray photoelectron spectroscopy (XPS) spectra of the $TiO_2/CuO/Cu_2O$ heterostructures with CuO/Cu_2O thickness of 20 nm (Cu20), decorated with Pd nanoparticles (red line) and reference layer (black line).
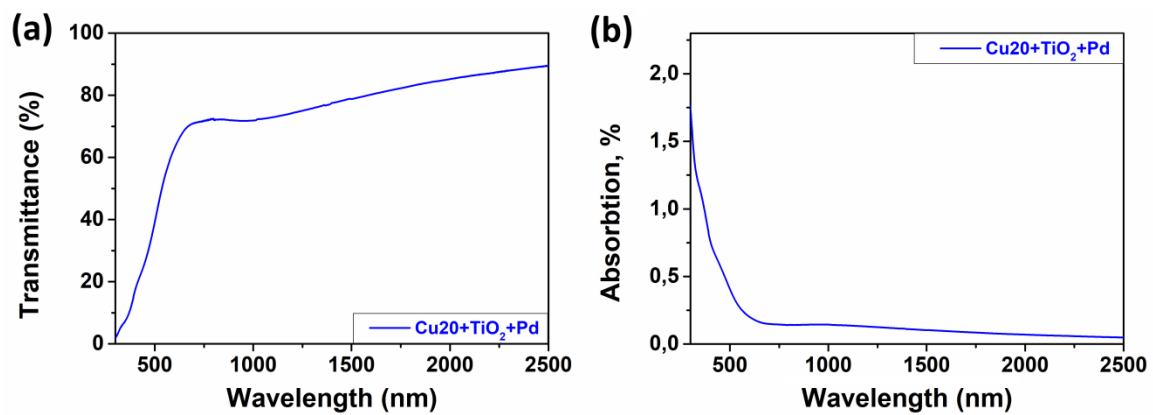
Figure S5. (a) Transmission spectra; and (b) Plot of absorption near the UV edge vs. wavelength of the Pd/TiO$_2$/CuO/Cu$_2$O heterostructure set sample with CuO/Cu$_2$O thickness of 20 nm annealed at 420 °C for 0.5 h.
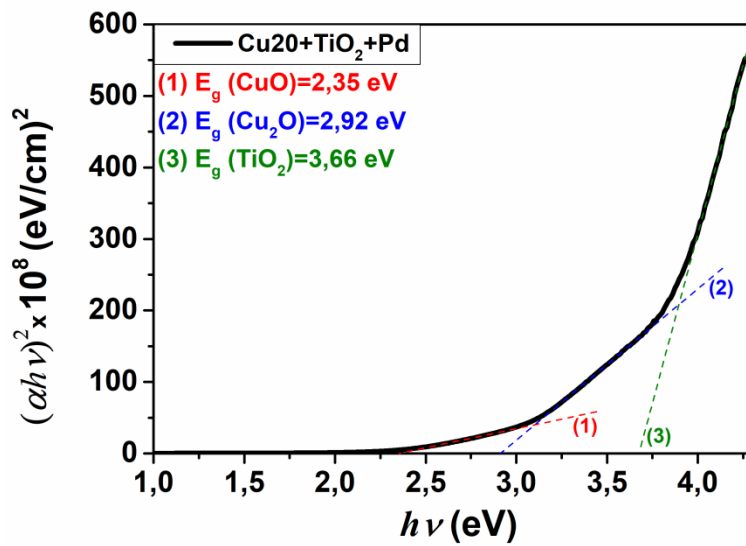
Figure S6. Plot of $(\alpha h\nu)^2$ vs. $h\nu$ for the copper oxide semiconductors in the substrate of Pd/TiO$_2$/CuO/Cu$_2$O.
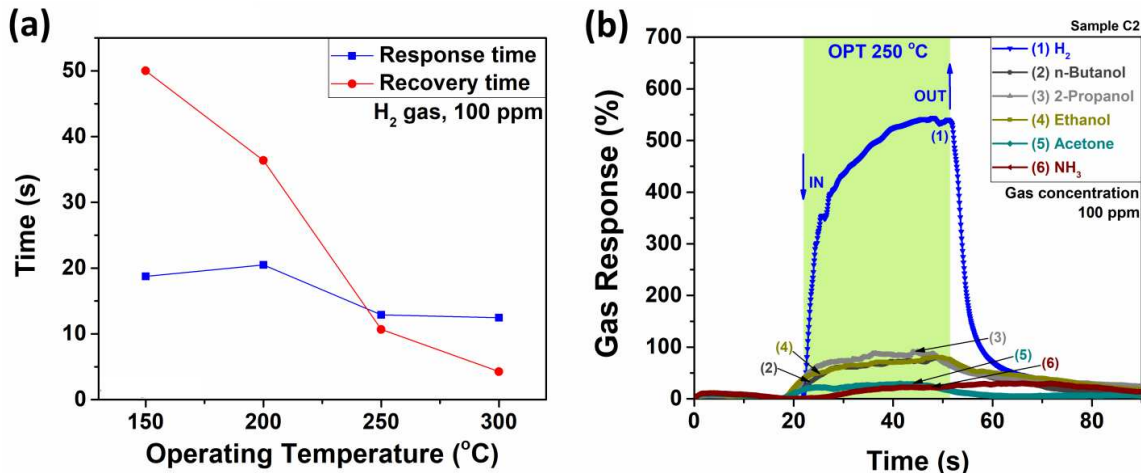
Figure S7. (a) Response / recovery times to 100 ppm of hydrogen at different operating temperatures of the TiO$_2$/CuO/Cu$_2$O samples with a CuO/Cu$_2$O thickness of 20 nm (Cu20) and decorated using Pd-NPs; (b) Dynamic response to different gases and volatiles (hydrogen, *n*-butanol, 2-propanol, ethanol, acetone, ammonia and CH$_4$) of the Pd-NPs/TiO$_2$/CuO/Cu$_2$O Cu20-samples at the operating temperature of 250 °C.
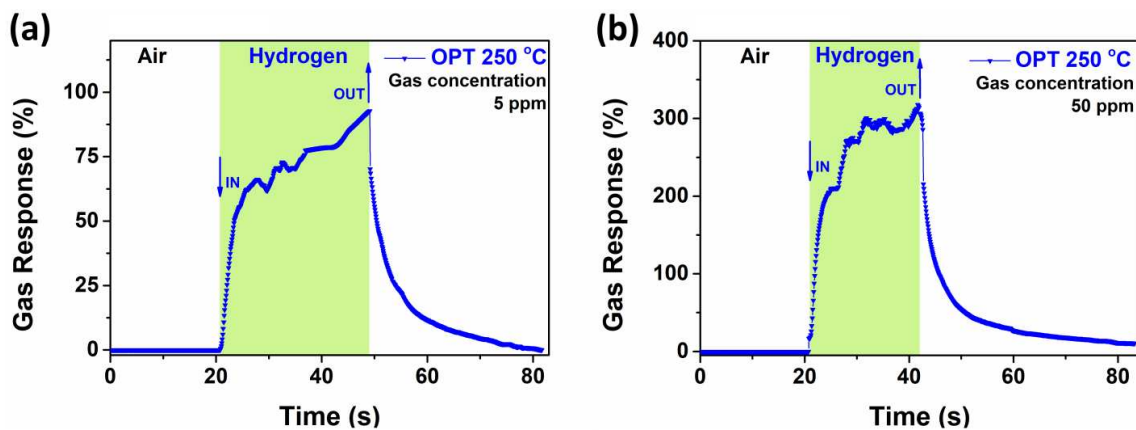
Figure S8. Dynamic response to: (a) 5 ppm; and (b) 50 ppm of hydrogen gas of the Pd-NPs/TiO$_2$/CuO/Cu$_2$O samples with a CuO/Cu$_2$O thickness of 20 nm (Cu20) at the operating temperature of 250 °C.
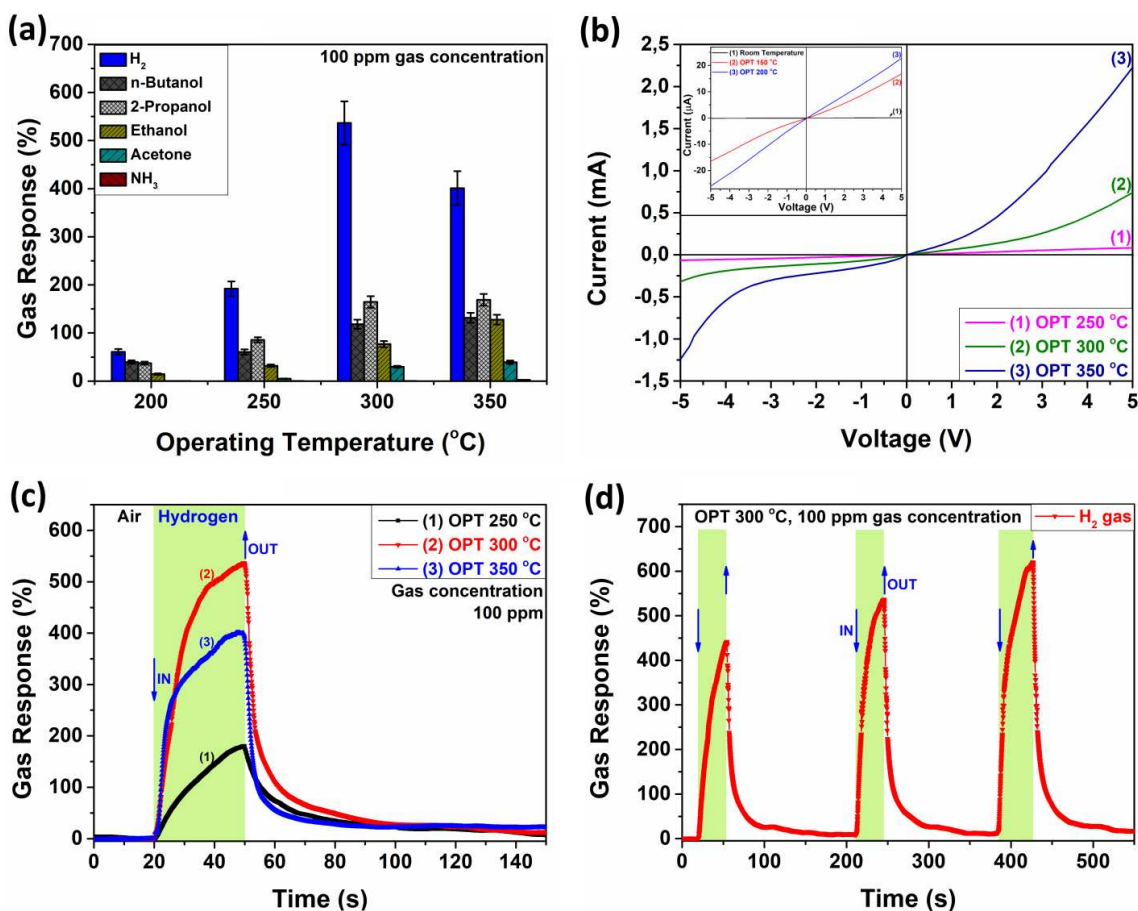
Figure S9. (a) Response to different gases and volatiles (hydrogen, *n*-butanol, ethanol, 2-propanol, acetone and ammonia) of the Pd/TiO$_2$/CuO/Cu$_2$O samples with a CuO/Cu$_2$O thickness of 30 nm (Cu30); (b) The *I-V* current-voltage characteristic of the Pd/TiO$_2$/CuO/Cu$_2$O samples with a CuO/Cu$_2$O thickness of 30 nm (Cu30) at the temperature of operation of 250 °C, 300 °C and 350 °C. The inset of the *I-V* current-voltage shows the behaviour of the same samples at low temperature of operation; (c) Dynamic response to hydrogen of the Pd/TiO$_2$/CuO/Cu$_2$O Cu30 samples at various temperatures of operation; (d) Dynamic response of the Pd-functionalized TiO$_2$/CuO/Cu$_2$O Cu30 samples to three consecutive pulses of hydrogen at the operating temperatures of 300 °C.
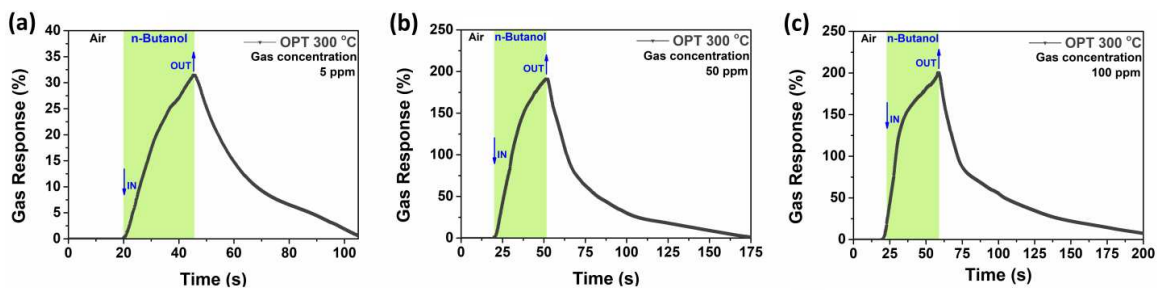
Figure S10. Dynamic response to: (a) 5 ppm; (b) 50 ppm; and (c) 100 ppm of *n*-butanol of the Ag-NPs/TiO$_2$/CuO/Cu$_2$O samples with a CuO/Cu$_2$O thickness of 60 nm (Cu60) at the temperature of operation of 300 °C.
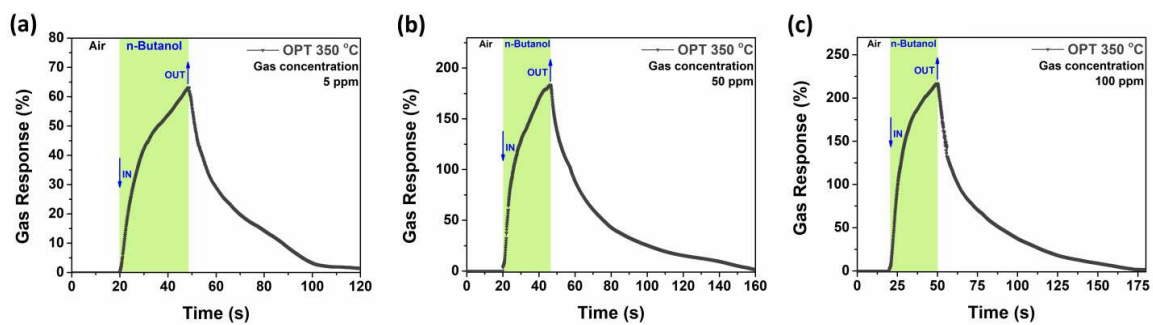
Figure S11. Dynamic response to: (a) 5 ppm; (b) 50 ppm; and (c) 100 ppm of *n*-butanol of the AgPt-NPs/TiO₂/CuO/Cu₂O samples with a CuO/Cu₂O thickness of 60 nm (Cu60) at the operating temperature of 300 °C.
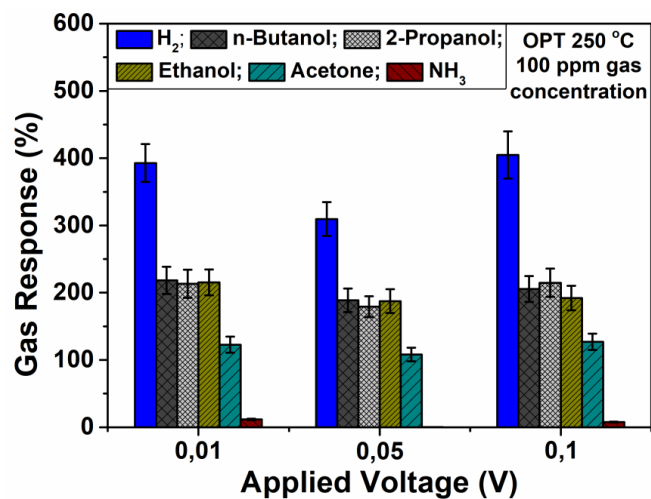
Figure S12. Response to different gases (hydrogen, *n*-butanol, 2-propanol, ethanol, acetone and ammonia) versus applied voltage of the Pd/TiO$_2$/CuO/Cu$_2$O samples with a CuO/Cu$_2$O thickness of 20 nm (Cu20).
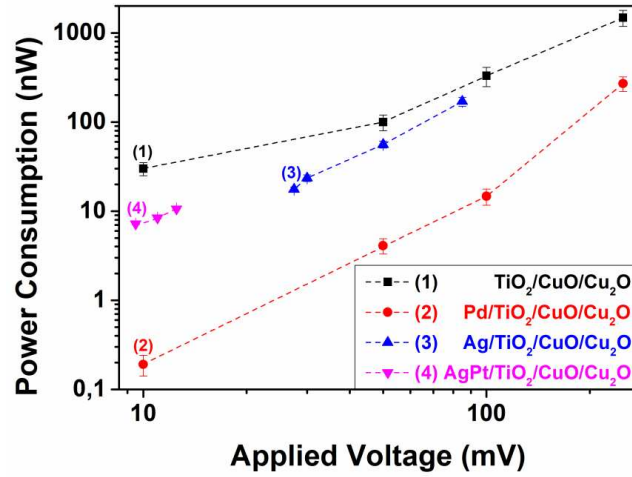
Figure S13. Dependence of the power consumption versus applied voltage for the $TiO_2/CuO/Cu_2O$ samples with a CuO/Cu_2O thickness of 20 nm (Cu20) and decorated using Pd, Ag or AgPt NPs.

Supporting Information Text S1

Heterostructures formed by *p-n* semiconductors, especially those functionalized with noble metals, have a highly efficient catalytic activity and can be used to enhance surface reactions in chemical sensing materials [1,2] and other applications [3–6]. Titania is known to be *n*-type semiconductor oxide [2,7,8], but mixed CuO/Cu_2O phases are *p*-type semiconductor oxides [9,10]. Thus, in $TiO_2/CuO/Cu_2O$ heterostructures it would normally appear that the main detection currents must flow through the TiO_2 layer. However, the resistance of the $TiO_2/CuO/Cu_2O$ heterostructures increases, as the detection currents are also influenced by the CuO/Cu_2O layer [2,11], which demonstrates a typical behavior of *p*-type semiconductor oxides [2,11].

Moreover, it is known that the functionalization of oxides (such as ZnO, SnO_2, TiO_2, Cu_2O and Fe_2O_3) with different noble metals and/or their alloys produces significant improvements of their sensing performances [2,11]. For specimens functionalized using nanoparticles (NPs) of noble metals or their oxides, the surface sensing mechanisms mainly follow to pathways [12,13]. The electrical sensitization mechanism takes place due to the formation of Schottky barriers at the nanojunction between the noble metal nanoparticles and the semiconductor oxide surface [14]. The chemical sensitization mechanism as a result of the new catalytic properties provided by the noble metals, which enhance the detection properties of gas sensors [12,15–19]. Thus, chemical sensitization facilitates the adsorption of certain gas molecules on the metal NP surface, which induces better interaction and reaction with pre-absorbed oxygen species, improving the gas detection performance [20,21].

Since we added Pd, Ag or AgPt NPs on the surfaces, more oxygen species are adsorbed via the "spillover effect", as was detected during the XPS studies (see Figure 3a,b and Figure S4). The good selectivity to hydrogen gas of the $Pd/TiO_2/CuO/Cu_2O$ heterostructures can be explained by the fact that Pd is known to be an excellent oxygen and hydrogen dissociation catalyst, even at low temperatures [13,15,22]. From the experimental data (Figure 4b), it can be observed that between relatively low operating temperatures and up to 200 °C, the signal recovery takes place more slowly than at high temperatures, as the adsorbed hydroxyl species (obtained during exposure to H_2) persist longer on the surface of the Pd NPs. The hydroxyl species are removed more slowly in the form of H_2O desorption at low than at high temperatures [23,24]. If the temperature is increased the oxygen spillover is predominant, since it is a thermally activated event [25].

In our case, the chemical sensitization is observed following the dissociation of hydrogen molecules over the reduced Pd NPs, forming atomic H with better reactivity:

$$H_{2(gas)} \xrightarrow{Pd} H_{(ads)} + H_{(ads)} \tag{S1}$$

$$H_{(ads)} + H_{(ads)} \rightarrow 2H_{(ads)}^+ + 2e^- \tag{S2}$$

indicating that the density of Pd NPs on the material surface is a highly important parameter [25].

As found in the XPS experiments of the PdO-functionalized WO_3-based sensors, the proton species (H^+) generated form palladium hydrides (PdH_x), which have lower work function in comparison to the pure Pd metal [26]:

$$xH_{(ads)}^+ + xe^- + Pd_{(s)} \rightarrow PdH_{x(s)} \tag{S3}$$

The formation of PdH$_x$ simplifies the transfer of charge carriers from the nanoparticles to the TiO$_2$/CuO/Cu$_2$O heterostructures and decreases the electron-depleted region, thus improving the gas detection value [15].

During the exposure of the Ag/TiO$_2$/CuO/Cu$_2$O or AgPt/TiO$_2$/CuO/Cu$_2$O heterostructures surfaces to *n*-butanol vapor, it reacts with oxygen species to form CO$_2$ and H$_2$O. The enhanced vapors sensing properties can be explained due to the unique properties of the heterostructures, that is the spillover and catalytic effects of the Ag and AgPt NPs [27]. In this process, the electrons are released from the oxygen species, reducing the size of the region with depletion of the electrons and the potential barriers. This process, which increases the resistance, is represented as [28–30]:

$$(C_4H_9OH)_{gas} \leftrightarrow (C_4H_9OH)_{ads} \tag{S4}$$

$$(C_4H_9OH)_{ads} + 12O^{2-}_{ads} \rightarrow 4CO_2 + 5H_2O + 24e^- \tag{S5}$$

$$(C_4H_9OH)_{ads} + 12O^-_{ads} \rightarrow 4CO_2 + 5H_2O + 12e^- \tag{S6}$$
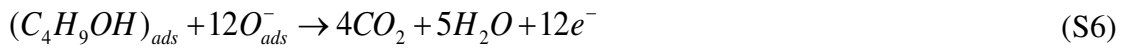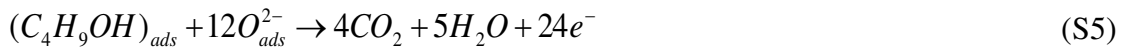
These concepts support the superiority of the gas sensing behavior of the Ag/TiO$_2$/CuO/Cu$_2$O or AgPt/TiO$_2$/CuO/Cu$_2$O heterostructures. Moreover, the large surface area of the crystals and the good catalytic performance of Ag and AgPt ensure a large number of active sites which facilitate the oxidation reaction of the VOC vapors. As a result, the gas can diffuse into the pores of the sensor, which increases the gas response.

The ternary $TiO_2(111)/CuO(\bar{1}11)/Cu_2O(111)$ heterojunction was modelled using a slab with an area of 125.512 Å^2 and containing 32 formula units (f.u.) of Cu_2O, 16 f.u. of CuO and 8 f.u. of TiO_2 dispersed over 12 atomic levels, see Figure 8. A vacuum gap of 20 Å was added in the direction perpendicular to the surface to avoid interaction between neighbouring cells.

The initial geometries for the monometallic nanoclusters were chosen based on the most thermodynamically stable structure, reported with the D_{5h} point group for isolated particles containing 7 transition metal atoms [31]. Figure S14a displays this shape consisting of 5 atoms occupying equatorial positions, which form a pentagon, and the remaining two atoms lying in the axial sites above and below the particle plane. We have selected this cluster size, as this is the smallest structure that can contain the Pt composition of approximately 15% closest to the one prepared in the experiments. For Ag_6Pt, we have used the configuration where the Pt is located at one of the axes of the cluster, since the occupation of the equatorial positions makes the system 162 meV higher in energy. Note that replacing one Ag by one Pt in Ag_6Pt reduces the symmetry of this nanoparticle to the C_{5v} point group. The Ag_6Pt particle was incorporated into the surface in such a way that the Pt atom was exposed, since we want to understand the chemical sensitisation of this element in the sensors. The transition metal clusters were added at the depression confined within the ring of TiO_2 units exposed at the top thin film in the ternary heterojunction, since they have similar sizes, offering a geometrically suitable anchor site. Following optimisation of the ternary heterostructures decorated with the nanoparticles, we found that the noble metal atoms did not stay in the geometry with

the D_{5h} point group, see Figures 8 and S14. Our simulations suggest that the noble metal occupying the axial position embedded into the ring of TiO_2 units, moving towards the heterostructure and further fixing the nanoparticle to the substrate. Following adsorption, the largest (least) elongation of the atoms lying at the opposite axial positions is calculated at 1.76 (1.18) Å for the Ag_7 (Pd_7) cluster. Replacing the exposed atom with Pt, equivalent to a concentration of 14.28% for this element, reduces the stretching of the axial atoms by 13.6% with respect to the parent nanoparticle. The adsorption of the clusters also caused distortions to the pentagons, *i.e.* 80% of the equatorial atoms moved 0.10 Å towards the axis of the Pd_7 cluster, while one of the Ag atoms moved 2.36 Å towards the vacuum, sitting at the same height of the axial atom in Ag_7. The pentagon of Ag_6Pt was the least affected and remained approximately flat after its incorporation into the surface of the heterojunction.
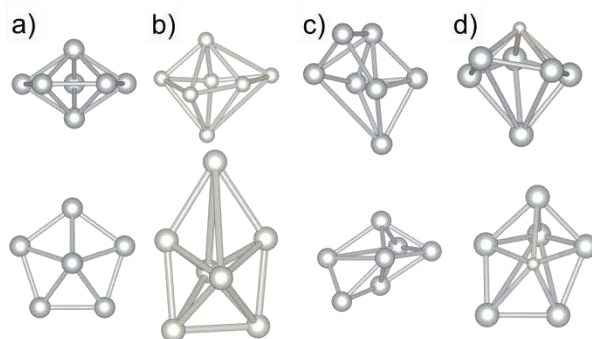
Figure S14. Equatorial view (top panels) and axial view (bottom panels) of: (a) an isolated nanoparticle containing 7 atoms in the D_{5h} point group, as well as (b) Pd_7; (c) Ag_7; and (d) Ag_6Pt clusters in their optimised adsorption configuration, where the heterostructure has been omitted for clarity. Pd, Pt as well as Pt atoms are in different shades of grey.

The Tersoff and Hamann scheme has been employed previously to realistically mimic experimental scanning tunnelling microscopy (STM) images [32–35], given that the tunnelling current is corresponding to the local density of states of the surface at the position of the tip. We have explored a range of positive and negative sample bias (V) and found that the addition of the noble metal nanoparticles modifies the valence bands around the Fermi level (E_F). For example, the incorporation of the Ag_7 cluster to the ternary heterojunction broadens by 0.5 eV the occupied electronic states of the material around the Fermi level. Swapping 14.3% of the Ag by Pt atoms further widens the valence bands of the sensor, requiring a sample bias of $V = -1.5$ eV. However, the Pd_7 cluster has a negligible effect on the density of states (DOS) of the hetero-epitaxial device, since a sample bias of $V = -0.5$ eV is needed both before and after surface functionalisation to force the flow of electrons from the valence band to the probe tip. Despite their different relaxed structures, our STM images suggest that all the noble metal clusters remain within the boundaries of a single dodecagon enclosed by TiO_2 units. The microscopy images also confirm that the deposition of the metal nanoparticles is feasible, if they at least fill 25% of the hollows enclosed by the exposed TiO_2 rings. The simulated STM images are not only in excellent agreement with the discussion of the adsorption structures of the nanoparticles, but they provide further insight into their different shapes, as a tool for differentiation.

We have used equation S7 to calculate the interfacial free energy (σ_{part}) of the nanoparticle functionalised hetero-epitaxial systems,

$$\sigma_{part} = \gamma_r + \left(E_{int} - \sum_{o=1}^{2} n_{over} E_{over} - E_{sub} - \sum_{p=1}^{2} n_{part} E_{part} \right) / A . \qquad (S7)$$

where γ_r is the relaxed surface energy of the Cu$_2$O(111) substrate; E_{int} and E_{sub} are the energies of the ternary interface and substrate, respectively; E_{over} is the energy of 1 f.u. in the bulk of the CuO($\bar{1}$11) and TiO$_2$(111) overlayers; and n_{over} is the number of f.u. in the overlayer; n_{part} represents the number of Ag, Pt and Pd atoms; E_{part} is the energy of one of such transition metal atoms in the *fcc* bulk; o represents the two overlayer phases; p is the maximum number of atom types in the nanoparticle and A is the surface area of one side of the slab.

Supporting Information Text S3

Table S1 reveals that the calculated interfacial free energy increases from the value of 112 meV·Å^{-2} for TiO$_2$(111)/CuO($\bar{1}$11)/Cu$_2$O(111) [9,36] after deposition of the transition metal particles. The chemical composition of the cluster plays a key role in the thermodynamic stability, since the most stable hetero-epitaxial junction in this study containing Ag$_7$ is 145 meV·Å^{-2} more stable than the least stable material decorated using Pd$_7$. Unsurprisingly, the deposition of the Ag$_6$Pt nanoalloy is slightly less favourable than the functionalisation using the pure Ag$_7$ parent cluster, since the interfacial free energy is only larger by 29 meV·Å^{-2}. The adsorption energy of the particles onto the ternary heterostructure was obtained from $E_{\text{ads}} = E_{\text{int+part}} - E_{\text{int}} - \sum_{p=1}^{2} n_{\text{part}} E_{\text{part}}$, which follows the same trend discussed for the interfacial free energy, as shown in Table S1. The positive value for the adsorption energy indicates that the cohesive forces are important to promote the growth of the transition metal clusters, rather than their disintegration wetting the surface of the device.

Table S1 also displays the charge transfer values (Δq), integrated using the Bader scheme [37–39], which suggest that all particles, and in particular the Ag-based ones, became positive upon adsorption. For the Ag$_6$Pt cluster, we found that each Ag atom donated +0.337 e$^-$ to the surface and Pt, which gained −0.307 e$^-$ in agreement with the relative electronegativities of these elements. The Ag$_7$ cluster has a negligible magnetic moment (m), which was also computed using the Bader methodology [37–39], since each positively charged atom has a full 4d shell, as reported in Table S1. However, Ag$_6$Pt and Pd$_7$ are magnetic, as the negatively charged Pt has a half-filled 6s level and the electronically depleted Pd has the electronic distribution 4d^9 with one unpaired electron.

The work function (Φ) is a property that provides evidence of the surface reactivity, as it quantifies the energy required to shift an electron from the Fermi level (E_F) to the potential of the vacuum (E_{vac}). The work function of the ternary heterojunction suffers a reduction of approximately 37% from its initial large value of $\Phi = 7.454$ eV after decoration using the noble metal nanoparticles, as listed in Table S1. The lower work function values calculated for the heterodevices after surface functionalisation explain their enhanced chemical reactivity, compared to these materials before adding the metal nanoclusters. Our simulated work function values have a small difference of up to 0.14 eV, suggesting that the composition of the nanoparticles can be used to finely tune the application of the materials as chemical sensors.

Table S1. Interfacial free energy (σ_{part}) and work function (Φ) for the ternary heterostructure $TiO_2(111)/CuO(\bar{1}11)/Cu_2O(111)$ decorated with the Pd_7, Ag_7 and Ag_6Pt clusters. The adsorption energy (E_{ads}), charge transfer (Δq) and magnetic moment (m) for the nanoparticles on the heterojunctions is also reported. Positive values of Δq indicate that the metal cluster loses electrons.

Cluster	Pd_7	Ag_7	Ag_6Pt
σ_{part} (meV·Å^{-2})	418	273	302
E_{ads} (eV)	4.302	0.779	2.249
Δq (e$^-$)	+1.127	+1.695	+1.717
m (μ_B)	0.418	0.014	0.891
Φ (eV)	4.825	4.798	4.681

Supporting Information Text S4

We have simulated the adsorption of a selection of the molecules examined during the gas response experiments, *i.e.* H_2, C_2H_5OH and *n*-C_4H_9OH, with the axial and equatorial positions of the transition metal clusters. Following previous works [35,40,41], we decided to introduce the H_2 molecule and the electron rich O atom from the VOCs at a distance of approximately 1.5 Å above the axial and equatorial adsorption sites of the noble metal particles. Moreover, the H from the OH polar functional group were oriented towards a nearby atom of the nanocluster, in order to maximize the number of interactions. All initial configurations were then allowed to relax to their equilibrium adsorption geometries and energies.

The binding energies for the interaction between the adsorbate molecules and the $TiO_2(111)/CuO(\bar{1}11)/Cu_2O(111)$ layered system functionalised with the Pd_7 nanoparticle are summarised in Table S2. Our calculations suggest that the most favourable binding configuration takes place when the H_2 molecule interacts with the equatorial Pd atom, releasing an adsorption energy of $E_{ads} = -1.494$ eV. However, the lowest and largest molecular weight alcohols prefer attaching to the equatorial and axial sites of the Pd_7 nanocluster, respectively. The calculated largest binding strength for *n*-C_4H_9OH (C_2H_5OH) is approximately 0.8 (0.6) eV lower than for H_2. The largest difference in adsorption energies between the equatorial and axial sites of the Pd_7 nanoparticle is 1.154 eV, which was calculated for the H_2 molecule. Furthermore, the alcohols showed the lowest variance of adsorption energies between the two Pd sites, with a value of just 0.017 eV for *n*-C_4H_9OH and only 22 times larger for C_2H_5OH. Despite the different

nature of the adsorbates, we observed an inverse relationship of their molecular weight with the change of adsorption energies between the equatorial and axial Pd positions.

Table S2. Adsorption energies (E_{ads}) and charge transfers (Δq) for H_2, C_2H_5OH and n-C_4H_9OH on the ternary heterojunction $TiO_2(111)/CuO(\bar{1}11)/Cu_2O(111)$ decorated with the Pd_7, Ag_7 and Ag_6Pt clusters. The adsorption site of the adsorbate on the nanoparticles is also indicated. A negative value of Δq denote that the adsorbate loses electronic charge.

Adsorbate	Site	Pd$_7$		Ag$_7$		Ag$_6$Pt	
		E_{ads} (eV)	Δq (e$^-$)	E_{ads} (eV)	Δq (e$^-$)	E_{ads} (eV)	Δq (e$^-$)
H_2	axial	−0.340	−0.046	**−0.282**	−0.039	−0.735	0.011
	equatorial	**−1.494**	0.319	0.178	−0.053	**−0.748**	−0.055
C_2H_5OH	axial	−0.515	−0.089	**−0.596**	−0.065	−0.395	−0.085
	equatorial	**−0.896**	−0.084	−0.579	−0.057	**−0.916**	−0.098
n-C_4H_9OH	axial	**−0.699**	−0.094	−0.560	−0.074	−0.852	−0.121
	equatorial	−0.682	−0.105	**−1.129**	−0.057	**−1.053**	−0.065

Table S2 also lists the adsorption energies released on $Ag_7/TiO_2(111)/CuO(\bar{1}11)/Cu_2O(111)$, displaying a strong shift in preference towards n-C_4H_9OH, where we calculated E_{ads} = −1.129 eV on the equatorial site. However, the adsorption of the largest molecular weight alcohol on the least coordinated axial site reduces its binding energy by around 50% compared to its equatorial Ag counterpart. C_2H_5OH releases E_{ads} = −0.596 and −0.579 eV when it interacts with the axial and equatorial positions, respectively, suggesting that this alcohol has a minor preference for the former adsorption site. We found that the non-polar H_2 molecule interacts weakly endothermically and exothermically with both the equatorial and axial Ag atoms,

respectively, with a difference in binding energies of *ca.* 0.5 eV. Our calculations reveal that the decreasing order of the molecular adsorption strength is $E_{ads}(n\text{-}C_4H_9OH) > E_{ads}(C_2H_5OH) > E_{ads}(H_2)$ after replacing the axial Ag atom by Pt in Ag_7, as shown in Table S2. However, the most favourable molecular interactions take place *via* the Ag sites, suggesting that the axial Pt species acts as a promoter of the equatorial atoms of the Ag_6Pt nanocluster. For the equatorial Ag binding position, we have elucidated the adsorption energy values of $E_{ads} = -1.053, -0.916$ and -0.748 eV for $n\text{-}C_4H_9OH$, C_2H_5OH and H_2, respectively. The smallest difference in adsorption energies between the axial Pt and equatorial Ag positions was found for H_2, which are almost degenerate at 0.013 eV. Inspection of the differences in binding energies between the two adsorption sites and the alcohols exhibits an inverse relationship with their molecular weights.

For the system containing the Pd_7 clusters, H_2 interacts molecularly and nearly vertically at 1.75 Å above the 5-fold axial Pd site (see Figure S15a), where it shows the least favourable adsorption observed on this material. The alcohols prefer to establish a single coordinate bond through their O with the axial Pd atom, but the molecules position themselves in different orientations with respect to the metal site. For example, C_2H_5OH moved outwards during the geometry optimisation from the initial equatorial site, forming a laterally coordinate bond of 2.27 Å to the axial Pd atom in its most stable adsorption configuration, as shown in Figure S15b. Despite the same O−Pd distance calculated for the interaction of C_2H_5OH with the two types of sites, the adsorbate remained atop the axial position of Pd_7 and further away from the sensor. The O atom from the largest molecular weight alcohol stayed above the initial adsorption site, *i.e.* at 2.23 and 2.13 Å from the axial and equatorial Pd sites, see Figure S15c. Our simulations

indicate that the short hydrocarbon chain of C_2H_5OH stays parallel to the surface, which, however, repels the longer alkyl radical of C_4H_9OH into a perpendicular configuration.

We have also analysed the atomic charges using the Bader partition scheme, which reveals that the VOCs on both adsorption sites and H_2 on the axial position of Pd_7 that lost electronic density, as shown in Table S2. For these interactions, the calculated charge transfers are below $\Delta q = -0.105$ e^- and their values are proportional to the molecular weight of the adsorbate. We found that the difference in charge transfer was 0.05 and 0.09 e^- for the two adsorption sites of n-C_4H_9OH and C_2H_5OH, respectively. Interestingly, the largest charge transfer for each VOC molecule was observed for the least favourable adsorption configuration. Unlike the alcohols, which lost charge density, in the most favourable interaction of the H_2 molecule with the equatorial position of Pd_7, we detected instead that the surface donated $\Delta q = 0.319$ e^- to the adsorbate. Our charge transfers suggest that electronic effects play a major role in the selectivity and sensitivity towards H_2 of the ternary heterojunction containing the Pd_7 clusters, which is essential to detect and discriminate this molecule within a mixture of VOCs.

Figure S15d-f illustrates the binding configurations of H_2, C_2H_5OH and n-C_4H_9OH on the most favourable adsorption sites of the $Ag_7/TiO_2(111)/CuO(\bar{1}11)/Cu_2O(111)$ system. The H_2 molecule adsorbs molecularly at approximately 2.0 Å above the axial and to the side of the equatorial sites of the Ag_7 nanocluster, see Figure S15d. The sensor can only exert a minor effect on the intramolecular H−H distance, with respect to the isolated H_2 molecule, which was calculated at 0.79 Å on both types of adsorption positions. We found that the C_2H_5OH molecule forms a vertical coordinate bond on the axial site with an O−Ag distance of 2.35 Å, which becomes 0.03 Å shorter at the equatorial adsorption

position, as shown in Figure S15e. The largest molecular weight alcohol interacts perpendicularly with the axial Ag atom at the slightly elongated distance of 2.31 Å. We observed that C_2H_5OH forms a flat adsorption configuration on both sites of the heterojunction decorated using the Ag_7 nanoparticles.

For the molecular adsorptions on the sensor decorated by the Ag_7 nanoparticles, the Bader charge transfers were calculated between −0.039 and −0.074 e⁻, see Table S2. These values indicate that the adsorbate loses electronic density to the heterojunction functionalised with the nanocluster, showing no clear correlation with the binding energies of the VOC and H_2 molecules. For example, the most thermodynamically favourable adsorption mode for n-C_4H_9OH at the equatorial position of the Ag_7 cluster displays an intermediate charge transfer of −0.057 e⁻. However, shifting this alcohol to its less stable adsorption site at the axial Ag increases the charge transfer to the largest value observed on this functionalised sensor. The H_2 molecule donates −0.053 e⁻ when it interacts endothermically with the equatorial Ag atom, while the charge transfer is reduced to −0.039 e⁻ on the axial adsorption site of the nanoparticle. Unlike n-C_4H_9OH and H_2, which experienced the largest charge flows in their least stable adsorption sites, C_2H_5OH preferred to donate −0.08 e⁻ more at the axial than at the equatorial adsorption site, in line with their different binding energies. The lack of agreement of the charge transfers with the molecular interaction strengths make are unable to explain the selectivity of the heterosensor decorated with the Ag_7 cluster for n-C_4H_9OH. Nevertheless, the small values of electron density flow that we have calculated for this material support the low sensitivity that it displayed in our experiments.
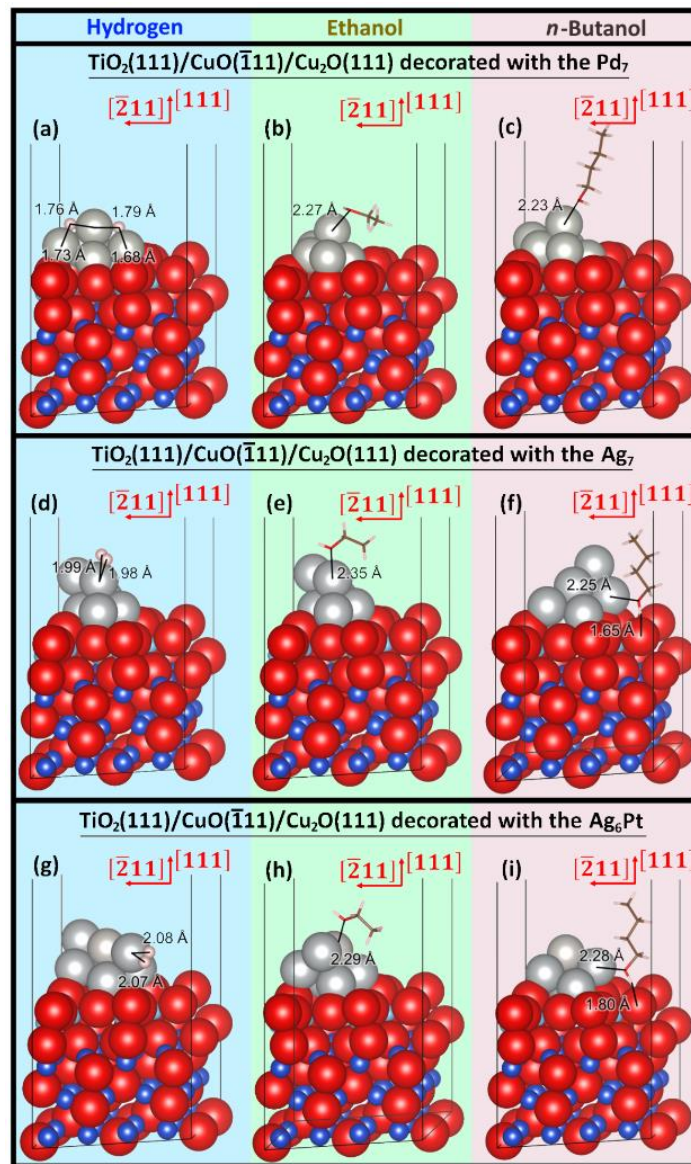
Figure S15. Adsorption of (a, c and g) H_2; (b, e and h) C_2H_5OH; and (c, f and i) *n*-C_4H_9OH on the heterostructure $TiO_2(111)/CuO(\bar{1}11)/Cu_2O(111)$ decorated with the (top panels) Pd_7, (middle panels) Ag_7 and (bottom panels) Ag_6Pt clusters. Interatomic distances are shown and crystallographic directions are indicated with respect to the $Cu_2O(111)$ substrate. The ternary heterojunctions functionalised using the noble metal nanoparticles are displayed using the space-filling representation, whereas the adsorbates are shown using the stick representation. O atoms are in red, H atoms are in white, C atoms are in brown, Cu atoms are in dark blue, Ti atoms are in light blue and Pd atoms are in grey.

Figure S15g-i depicts the structures of the molecular interactions with the surface sites of the hetero-epitaxial material decorated with Ag_6Pt that released the largest adsorption energies. We found that H_2 remained perpendicularly atop the axial Pt atom at 1.91 Å, while it coordinated laterally to the equatorial Ag site at the more elongated distance of 2.07 Å, which moved outwards upon adsorption, see Figure S15g. Our DFT modelling suggests that C_2H_5OH prefers to stay parallel to the surface, binding both adsorption sites at the same distance of 2.29 Å, regardless of the different chemical nature of the metal atom, as shown in Figure S15h. Moving this alcohol to the axial site forces a reduction of the interfacial O−Pt distance to 2.23 Å, which is nevertheless insufficient to counteract the loss of the hydrogen-bond formed at the equatorial Ag site.

Our calculated charge transfers indicate that most of the adsorbates donate electronic density to the sensor containing the Ag_6Pt nanoclusters, see Table S2. The electronic charges transferred by C_2H_5OH to the axial and equatorial sites of the nanoparticle are −0.085 and −0.098 e^-, respectively, displaying a direct correlation with the adsorption energies released in these positions. In contrast, n-C_4H_9OH donated −0.065 e^- in the most stable adsorption configuration on Ag_6Pt, a value that nearly doubled at the axial Pt position, leading to the largest charge transfer on this system. Despite H_2 having very close binding energies on both adsorption sites of Ag_6Pt, our models suggest that those interactions have opposite flows of electronic density, with the molecule receiving a charge of 0.011 e^- in the axial position.

In this work, we have simulated the adsorption energies for the VOCs and H_2 and found them to follow the same trends of our gas response experiments for the heterodevices

functionalised with nanoparticles. The positive charge for the noble metal clusters was calculated within the +1.1 to +1.7 e^- range, which lies between the values obtained for the cations of the pristine binary and ternary heterojunctions. Our simulations suggest that C_2H_5OH lies parallel to the surface of the sensor, due to its short alkyl radical, only allowing coordination between the molecular O atom and the noble metal. This results in the weakest interactions calculated for the two alcohols investigated computationally here, which compares well with our gas sensing experiments. However, the average distance between the equatorial atom of the nanoparticle and the closest surface O atom from the TiO_2 is 4.22 Å. Thus, we observed the formation of an additional hydrogen-bond between the Ag-based nanoparticles and n-C_4H_9OH, since its large alkyl radical accommodates itself perpendicularly to the surface, leading to the largest adsorption energies calculated on these systems. We have also shown that there is a concomitant effect between the reduction of the positive charge and the work function for the exposed atoms in the heterojunctions after functionalisation using the metallic nanoparticles. The intermediate atomic charge of the metallic nanoparticles induces a reduction of the work functions with respect to the binary and ternary heterojunctions. The work function descriptor justifies the large sensitivity of the $Pd_7/TiO_2(111)/CuO(\bar{1}11)/Cu_2O(111)$ sensor towards H_2, since it received $\Delta q = -0.319$ e^- from the surface, which allowed its dissociation, releasing the largest exothermic adsorption energy of this study, in excellent agreement with our gas sensing experiments. The quantum mechanical calculations presented here support, complement and explain the changes of selectivity and sensitivity found in our experiments for the ternary $TiO_2(111)/CuO(\bar{1}11)/Cu_2O(111)$ heteroepitaxial junction after decoration using the Pd_7, Ag_7 and Ag_6Pt nanoparticles.

We have performed DFT+U−D3(BJ) simulations to interrogate the properties of the TiO$_2$(111)/CuO($\bar{1}$11)/Cu$_2$O(111) heterostructure decorated with the Pd$_7$, Ag$_7$ and Ag$_6$Pt nanoparticles as well as their interaction with H$_2$, C$_2$H$_5$OH and n-C$_4$H$_9$OH. We have explained the incorporation of pentagonal nanoparticles in their ground state symmetry, *i.e.* D_{5h} point group for the monometallic systems and the reduced C_{5v} point group for the Ag$_6$Pt nanoalloy, onto the depressions existing in the TiO$_2$(111) layer. We have found positive values for the adsorption energies, indicating that cohesive forces drive the growth of the mono- and bi-metallic nanoparticles. The surface free energy of the heteroepitaxial material rises as a result of the deposition of the nanoparticles, suggesting that the decoration process reduces the stability of the sensor. However, the adsorption of the nanoparticles leads to lower values of the work function, which explains the enhanced sensing properties of the material, in agreement with experiments. The most favourable interaction was calculated for dissociative adsorption of H$_2$ on the sensor containing the Pd$_7$ nanoparticles, since the molecule receives charge from the sensor. The large alkyl radical of the n-C$_4$H$_9$OH molecule positions itself perpendicular to the surface, allowing the formation of additional hydrogen-bond interactions with the surface oxygen when the surface of the heterodevice is decorated using the Ag-based nanoparticles. The small C$_2$H$_5$OH molecule always adsorbs parallel, which prevents the formation of a secondary coordination bonds to the surface.

Figure S16 displays the atomic projections of the spin decomposed electronic density of states (PDOS) for the topmost TiO$_2$ layer of the pristine and noble metal nanocluster modified ternary heterojunctions. Before addition of any nanoparticle, the valence band of the TiO$_2$ layer is dominated by the 2p levels of the O atoms between the Fermi level

and −4.5 eV, see Figure S16a. The 3*d* states of the Ti atoms appear in the conduction band with the minimum located at 2.9 eV. We also found a small unoccupied band in the minority channel of the spins due to the O *p* orbitals at around 1.5 eV. Our calculated electronic structures suggest that the impregnation of the nanoparticles enhances the PDOS of the occupied Ti 3*d* states with the center roughly located at −2.5 eV as shown in Figure S16b to S16d. The functionalization of the heterojunction with any of the three metal nanoclusters also lowers significantly the occupied bands of the 2*p* states of the O atoms.
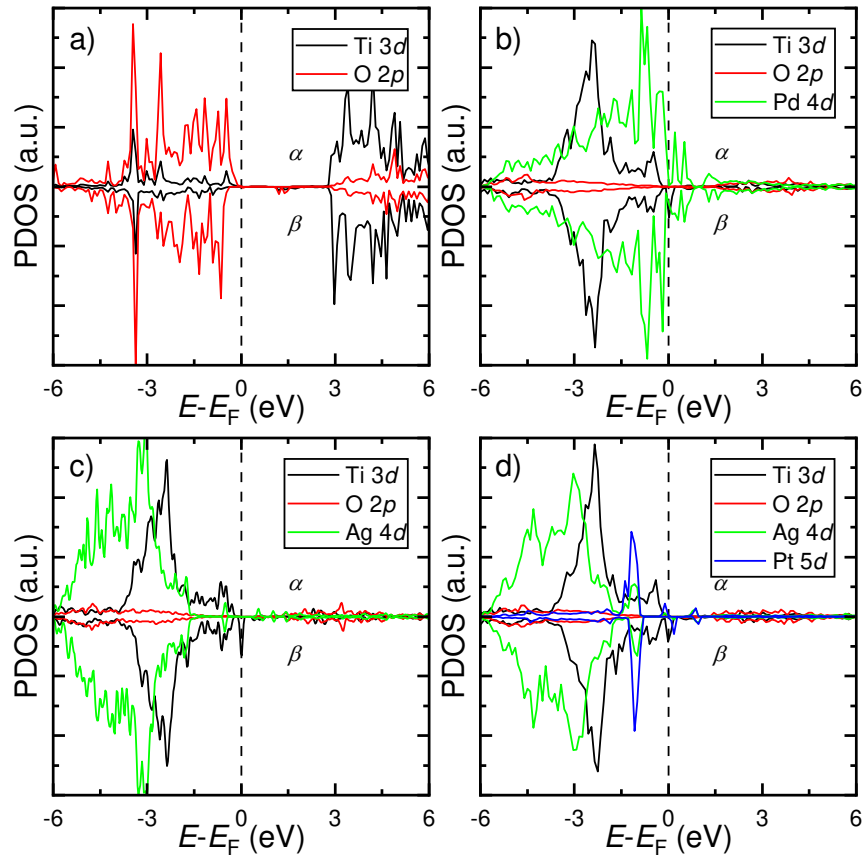

Figure S16. Atomic projections of the spin decomposed electronic density of states (PDOS) for the topmost TiO_2 layer of: (a) the pristine ternary heterojunction and after deposition of the (b) Pd_7; (c) Ag_7; and (d) Ag_6Pt nanoclusters. α and β stand for the majority and minority channels of the spins.

The main difference between the PDOS of the functionalized heteroepitaxial junctions lies in the position of the d bands of the noble metal atoms. When Pd_7 is decorating the surface, the partially occupied Pd $4d$ states appear between -6.0 and 1.0 eV, see Figure S16b. However, when Pd is replaced by Ag, the $4d$ bands of the noble metal are pushed to lower values of energy, with the maximum now located at -1.7 eV as shown in Figure S16c. Swapping one of the Ag atoms by Pt in Ag_7 do not change significantly the PDOS of the former, but a new narrow band appear at -1.0 eV due to the $5d$ states of the latter, see Figure S16d.

Figure S17 shows the gas response of a Pd functionalized sensor at relative humidity (RH) of 17% and 67%. We can see that the signals are in good agreement, showing that moisture from the air is not detrimental to the functionality of the sensor system.
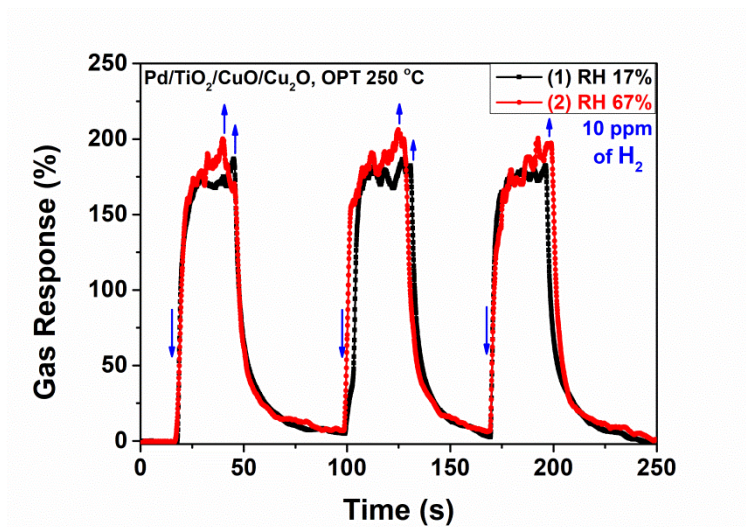

Figure S17. Dynamic response to 10 ppm of hydrogen in air of the $Pd/TiO_2/CuO/Cu_2O$ samples at different relative humidity (RH) values.

References

[1]   V. Postica, A. Vahl, N. Magariu, M.-I. Terasa, M. Hoppe, B. Viana, P. Aschehoug, T. Pauporté, I. Tiginyanu, O. Polonskyi, V. Sontea, L. Chow, L. Kienle, R. Adelung, F. Faupel, O. Lupan, Enhancement in UV Sensing Properties of ZnO:Ag Nanostructured Films by Surface Functionalization with Noble Metalic and Bimetallic Nanoparticles, J. Eng. Sci. XXV (2018) 41–51. https://doi.org/10.5281/zenodo.2557280.

[2]   N. Ababii, M. Hoppe, S. Shree, A. Vahl, M. Ulfa, T. Pauporté, B. Viana, V. Cretu, N. Magariu, V. Postica, V. Sontea, M.-I. Terasa, O. Polonskyi, F. Faupel, R. Adelung, O. Lupan, Effect of noble metal functionalization and film thickness on sensing properties of sprayed TiO_2 ultra-thin films, Sensors Actuators A Phys. 293 (2019) 242–258. https://doi.org/10.1016/j.sna.2019.04.017.

[3]   X. Wang, R. Yu, C. Jiang, W. Hu, W. Wu, Y. Ding, W. Peng, S. Li, Z.L. Wang, Piezotronic Effect Modulated Heterojunction Electron Gas in AlGaN/AlN/GaN Heterostructure Microwire, Adv. Mater. 28 (2016) 7234–7242. https://doi.org/10.1002/adma.201601721.

[4]   Y. Eso, A. Takai, T. Matsumoto, T. Inuzuka, T. Horie, K. Ono, S. Uemoto, K. Lee, W. Edelmann, T. Chiba, H. Marusawa, M_SH_2 Dysregulation Is Triggered by Proinflammatory Cytokine Stimulation and Is Associated with Liver Cancer Development, Cancer Res. 76 (2016) 4383–4393. https://doi.org/10.1158/0008-5472.CAN-15-2926.

[5]   F. Xue, L. Yang, M. Chen, J. Chen, X. Yang, L. Wang, L. Chen, C. Pan, Z.L. Wang, Enhanced photoresponsivity of the MoS_2-GaN heterojunction diode via the piezo-phototronic effect, NPG Asia Mater. 9 (2017) e418–e418. https://doi.org/10.1038/am.2017.142.

[6]   M. Mathew, P. V Shinde, R. Samal, C.S. Rout, A review on mechanisms and recent developments in p-n heterojunctions of 2D materials for gas sensing applications, J. Mater. Sci. 56 (2021) 9575–9604. https://doi.org/10.1007/s10853-021-05884-4.

[7]   A. Mattsson, L. Österlund, Adsorption and Photoinduced Decomposition of Acetone and Acetic Acid on Anatase, Brookite, and Rutile TiO_2 Nanoparticles, J.

Phys. Chem. C. 114 (2010) 14121–14132. https://doi.org/10.1021/jp103263n.

[8]   B.J. Morgan, G.W. Watson, Intrinsic n-type Defect Formation in TiO_2: A Comparison of Rutile and Anatase from GGA+ U Calculations, J. Phys. Chem. C. 114 (2010) 2321–2328. https://doi.org/10.1021/jp9088047.

[9]   O. Lupan, V. Cretu, V. Postica, N. Ababii, O. Polonskyi, V. Kaidas, F. Schütt, Y.K. Mishra, E. Monaico, I. Tiginyanu, V. Sontea, T. Strunskus, F. Faupel, R. Adelung, Enhanced ethanol vapour sensing performances of copper oxide nanocrystals with mixed phases, Sensors Actuators B Chem. 224 (2016) 434–448. https://doi.org/10.1016/j.snb.2015.10.042.

[10]   O. Lupan, V. Cretu, V. Postica, O. Polonskyi, N. Ababii, F. Schütt, V. Kaidas, F. Faupel, R. Adelung, Non-planar nanoscale p–p heterojunctions formation in $Zn_xCu_{1-x}O_y$ nanocrystals by mixed phases for enhanced sensors, Sensors Actuators B Chem. 230 (2016) 832–843. https://doi.org/10.1016/j.snb.2016.02.089.

[11]   H. Xuemei, S. Yukun, B. Bo, Fabrication of Cubic p-n Heterojunction-Like NiO/In_2O_3 Composite Microparticles and Their Enhanced Gas Sensing Characteristics, J. Nanomater. 2016 (2016) 1–9. https://doi.org/10.1155/2016/7589028.

[12]   N. Yamazoe, New approaches for improving semiconductor gas sensors, Sensors Actuators B Chem. 5 (1991) 7–19. https://doi.org/10.1016/0925-4005(91)80213-4.

[13]   A. Kolmakov, D.O. Klenov, Y. Lilach, S. Stemmer, M. Moskovits, Enhanced Gas Sensing by Individual SnO_2 Nanowires and Nanobelts Functionalized with Pd Catalyst Particles, Nano Lett. 5 (2005) 667–673. https://doi.org/10.1021/nl050082v.

[14]   D. Acharyya, K.Y. Huang, P.P. Chattopadhyay, M.S. Ho, H.-J. Fecht, P. Bhattacharyya, Hybrid 3D structures of ZnO nanoflowers and PdO nanoparticles as a highly selective methanol sensor, Analyst. 141 (2016) 2977–2989. https://doi.org/10.1039/C6AN00326E.

[15]   O. Lupan, V. Postica, M. Hoppe, N. Wolff, O. Polonskyi, T. Pauporté, B. Viana, O. Majérus, L. Kienle, F. Faupel, R. Adelung, PdO/PdO_2 functionalized ZnO:Pd films for lower operating temperature H_2 gas sensing, Nanoscale. 10 (2018) 14107–14127. https://doi.org/10.1039/C8NR03260B.

[16] D. Zhao, M. Dai, Y. Zhao, H. Liu, Y. Liu, X. Wu, Improving electrocatalytic activities of $FeCo_2O_4$@$FeCo_2S_4$@PPy electrodes by surface/interface regulation, Nano Energy. 72 (2020) 104715. https://doi.org/10.1016/j.nanoen.2020.104715.

[17] D. Zhao, H. Liu, X. Wu, Bi-interface induced multi-active MCo_2O_4@MCo_2S_4@PPy (M=Ni, Zn) sandwich structure for energy storage and electrocatalysis, Nano Energy. 57 (2019) 363–370. https://doi.org/10.1016/j.nanoen.2018.12.066.

[18] D. Zhao, M. Dai, H. Liu, K. Chen, X. Zhu, D. Xue, X. Wu, J. Liu, Sulfur-Induced Interface Engineering of Hybrid $NiCo_2O_4$@$NiMo_2S_4$ Structure for Overall Water Splitting and Flexible Hybrid Energy Storage, Adv. Mater. Interfaces. 6 (2019) 1901308. https://doi.org/10.1002/admi.201901308.

[19] H. Liu, D. Zhao, Y. Liu, P. Hu, X. Wu, H. Xia, Boosting energy storage and electrocatalytic performances by synergizing $CoMoO_4$@$MoZn_{22}$ core-shell structures, Chem. Eng. J. 373 (2019) 485–492. https://doi.org/10.1016/j.cej.2019.05.066.

[20] J.-H. Kim, P. Wu, H.W. Kim, S.S. Kim, Highly Selective Sensing of CO, C_6H_6, and C_7H_8 Gases by Catalytic Functionalization with Metal Nanoparticles, ACS Appl. Mater. Interfaces. 8 (2016) 7173–7183. https://doi.org/10.1021/acsami.6b01116.

[21] S.M. Majhi, A. Mirzaei, H.W. Kim, S.S. Kim, T.W. Kim, Recent advances in energy-saving chemiresistive gas sensors: A review, Nano Energy. 79 (2021) 105369. https://doi.org/10.1016/j.nanoen.2020.105369.

[22] N. Yamazoe, New approaches for improving semiconductor gas sensors, Sensors Actuators B Chem. 5 (1991) 7–19. https://doi.org/10.1016/0925-4005(91)80213-4.

[23] Y.T. Lee, J.M. Lee, Y.J. Kim, J.H. Joe, W. Lee, Hydrogen gas sensing properties of PdO thin films with nano-sized cracks, Nanotechnology. 21 (2010) 165503. https://doi.org/10.1088/0957-4484/21/16/165503.

[24] Y.-J. Chiang, K.-C. Li, Y.-C. Lin, F.-M. Pan, A mechanistic study of hydrogen gas sensing by PdO nanoflake thin films at temperatures below 250 °C, Phys. Chem. Chem. Phys. 17 (2015) 3039–3049. https://doi.org/10.1039/C4CP04527K.

[25] C.-M. Chang, M.-H. Hon, I.-C. Leu, Outstanding H_2 Sensing Performance of Pd

Nanoparticle-Decorated ZnO Nanorod Arrays and the Temperature-Dependent Sensing Mechanisms, ACS Appl. Mater. Interfaces. 5 (2013) 135–143. https://doi.org/10.1021/am302294v.

[26] F.E. Annanouch, Z. Haddi, M. Ling, F. Di Maggio, S. Vallejos, T. Vilic, Y. Zhu, T. Shujah, P. Umek, C. Bittencourt, C. Blackman, E. Llobet, Aerosol-Assisted CVD-Grown PdO Nanoparticle-Decorated Tungsten Oxide Nanoneedles Extremely Sensitive and Selective to Hydrogen, ACS Appl. Mater. Interfaces. 8 (2016) 10413–10421. https://doi.org/10.1021/acsami.6b00773.

[27] B. Yang, J. Liu, H. Qin, Q. Liu, X. Jing, H. Zhang, R. Li, G. Huang, J. Wang, PtO$_2$ -nanoparticles functionalized CuO polyhedrons for n-butanol gas sensor application, Ceram. Int. 44 (2018) 10426–10432. https://doi.org/10.1016/j.ceramint.2018.03.059.

[28] M. Kanerva, L.-S. Johansson, J.M. Campbell, H. Revitzer, E. Sarlin, T. Brander, O. Saarela, Hydrofluoric–nitric–sulphuric-acid surface treatment of tungsten for carbon fibre-reinforced composite hybrids in space applications, Appl. Surf. Sci. 328 (2015) 418–427. https://doi.org/https://doi.org/10.1016/j.apsusc.2014.12.036.

[29] X. Liu, N. Chen, X. Xing, Y. Li, X. Xiao, Y. Wang, I. Djerdj, A high-performance n-butanol gas sensor based on ZnO nanoparticles synthesized by a low-temperature solvothermal route, RSC Adv. 5 (2015) 54372–54378. https://doi.org/10.1039/C5RA05148G.

[30] Y. V Kaneti, Q.M.D. Zakaria, Z. Zhang, C. Chen, J. Yue, M. Liu, X. Jiang, A. Yu, Solvothermal synthesis of ZnO-decorated α-Fe$_2$O$_3$ nanorods with highly enhanced gas-sensing performance toward n-butanol, J. Mater. Chem. A. 2 (2014) 13283–13292. https://doi.org/10.1039/C4TA01837K.

[31] T. Lazauskas, A.A. Sokol, J. Buckeridge, C.R.A. Catlow, S.G.E.T. Escher, M.R. Farrow, D. Mora-Fonz, V.W. Blum, T.M. Phaahla, H.R. Chauke, P.E. Ngoepe, S.M. Woodley, Thermodynamically accessible titanium clusters Ti$_N$, N = 2-32, Phys. Chem. Chem. Phys. 20 (2018) 13962–13973. https://doi.org/10.1039/c8cp00406d.

[32] D. Santos-Carballal, A. Roldan, R. Grau-Crespo, N.H. de Leeuw, A DFT study of the structures, stabilities and redox behaviour of the major surfaces of magnetite

Fe_3O_4, Phys. Chem. Chem. Phys. 16 (2014) 21082–21097. https://doi.org/10.1039/c4cp00529e.

[33] A.E. Shields, D. Santos-Carballal, N.H. de Leeuw, A density functional theory study of uranium-doped thoria and uranium adatoms on the major surfaces of thorium dioxide, J. Nucl. Mater. 473 (2016) 99–111. https://doi.org/10.1016/j.jnucmat.2016.02.009.

[34] M.J. Ungerer, D. Santos-Carballal, A. Cadi-Essadek, C.G.C.E. van Sittert, N.H. de Leeuw, Interaction of H_2O with the Platinum Pt (001), (011), and (111) Surfaces: A Density Functional Theory Study with Long-Range Dispersion Corrections, J. Phys. Chem. C. 123 (2019) 27465–27476. https://doi.org/10.1021/acs.jpcc.9b06136.

[35] V. Postica, A. Vahl, J. Strobel, D. Santos-Carballal, O. Lupan, A. Cadi-Essadek, N.H. De Leeuw, F. Schütt, O. Polonskyi, T. Strunskus, M. Baum, L. Kienle, R. Adelung, F. Faupel, Tuning doping and surface functionalization of columnar oxide films for volatile organic compounds sensing: Experiments and theory, J. Mater. Chem. A. 6 (2018) 23669–23682. https://doi.org/10.1039/C8TA08985J.

[36] V. Cretu, V. Postica, A.K. Mishra, M. Hoppe, I. Tiginyanu, Y.K. Mishra, L. Chow, N.H. de Leeuw, R. Adelung, O. Lupan, Synthesis, characterization and DFT studies of zinc-doped copper oxide nanocrystals for gas sensing applications, J. Mater. Chem. A. 4 (2016) 6527–6539. https://doi.org/10.1039/C6TA01355D.

[37] G. Henkelman, A. Arnaldsson, H. Jónsson, A fast and robust algorithm for Bader decomposition of charge density, Comput. Mater. Sci. 36 (2006) 354–360. https://doi.org/10.1016/j.commatsci.2005.04.010.

[38] E. Sanville, S.D. Kenny, R. Smith, G. Henkelman, Improved grid-based algorithm for Bader charge allocation., J. Comput. Chem. 28 (2007) 899–908. https://doi.org/10.1002/jcc.20575.

[39] W. Tang, E. Sanville, G. Henkelman, A grid-based Bader analysis algorithm without lattice bias., J. Phys. Condens. Matter. 21 (2009) 084204. https://doi.org/10.1088/0953-8984/21/8/084204.

[40] A. Vahl, O. Lupan, D. Santos-Carballal, V. Postica, S. Hansen, H. Cavers, N. Wolff, M.-I. Terasa, M. Hoppe, A. Cadi-Essadek, T. Dankwort, L. Kienle, N.H. de

Leeuw, R. Adelung, F. Faupel, Surface functionalization of ZnO:Ag columnar thin films with AgAu and AgPt bimetallic alloy nanoparticles as an efficient pathway for highly sensitive gas discrimination and early hazard detection in batteries, J. Mater. Chem. A. 8 (2020) 16246–16264. https://doi.org/10.1039/D0TA03224G.

[41]   V. Postica, A. Vahl, D. Santos-Carballal, T. Dankwort, L. Kienle, M. Hoppe, A. Cadi-Essadek, N.H. de Leeuw, M.-I. Terasa, R. Adelung, F. Faupel, O. Lupan, Tuning ZnO Sensors Reactivity toward Volatile Organic Compounds via Ag Doping and Nanoparticle Functionalization, ACS Appl. Mater. Interfaces. 11 (2019) 31452–31466. https://doi.org/10.1021/acsami.9b07275.